ADVANCED FUNCTIONAL MATERIALS
www.afm-journal.de

Ultrafine Amorphous SnO_x Embedded in Carbon Nanofiber/Carbon Nanotube Composites for Li-Ion and Na-Ion Batteries

*Biao Zhang, Jiaqiang Huang, and Jang-Kyo Kim**

Core–shell-structured, ultrafine SnO_x/carbon nanofiber (CNF)/carbon nanotube composite films are in situ synthesized by electrospinning through a dual nozzle. The carbon shell layer functions as a buffer to prevent the separation of SnO_x particles from the CNF core, allowing full utilization of high-capacity SnO_x in both Li-ion and Na-ion batteries. The composite electrodes reveal an anomalous Li- and Na-ion storage mechanism where all the intermediate phases, like Li_xSn and Na_xSn alloys, maintain amorphous states during the entire charge/discharge process. The uniform dispersion on an atomic scale and the amorphous state of the SnO_x particles remain intact in the carbon matrix without growth or crystallization even after 300 cycles, which is responsible for sustaining excellent capacity retention of the electrodes. These discoveries not only shed new insights into fundamental understanding of the electrochemical behavior of SnO_x electrodes but also offer a potential strategy to improve the cyclic stability of other types of alloy anodes that suffer from rapid capacity decays due to large volume changes.

1. Introduction

The world is currently experiencing energy challenges on two main fronts: namely, i) shifting production of electricity from burning fossil fuels to harvesting sustainable energy sources; and ii) driving transportation systems from vehicles with internal combustion engines toward electric vehicles (EVs). These challenges have led to increasing demands for developing more efficient and cost-effective energy storage systems with powerful, consistent outputs and long life.[1] Li-ion batteries (LIBs) have achieved great success in powering portable electronics. They have also been extensively explored to further enhance their energy/power densities while reducing the fabrication/material costs for application in EVs, where emerging Na-ion batteries (NIBs) could be a potential competitor. Although NIBs in general have lower energy/power densities than LIBs because of the higher potential of Na/Na^+ (−2.7 V vs −3.0 V for Li/Li^+) and larger radius of Na ions (0.98 Å vs 0.69 Å for Li ions), the low cost and abundant availability of sodium source make them very attractive for EVs and stationary energy storage.[2] Developing high-performance electrode materials that possess high capacities and long-term stability is essential to successful commercialization of both batteries for EVs.

SnO_x has been widely studied as promising candidates for replacing graphite anode in LIBs because of its high theoretical capacity and suitable plateau to avoid the deposition of metallic lithium.[3] Moreover, SnO_x is reported to be an attractive anode for NIBs through the conversion of SnO_x into Sn/Na_2O and alloying of Sn with Na, similar to those occurring in Li storage.[4] One of the main challenges to its practical application is the poor cyclic performance arising from huge volume changes of SnO_x. Many strategies have thus been proposed to improve the cyclic performance of SnO_x anodes, among which the incorporation of nanocarbon materials into the SnO_x anodes is proven to be the most effective. Encapsulation of SnO_x nanoparticles into nanocarbon materials, such as graphene, porous carbon, carbon nanotubes (CNTs), and carbon nanofibers (CNFs), could not only alleviate the volume change but also facilitate fast charge transfer through the highly conductive carbon matrix.[5,6] The aggregation of metal oxides and separation of active materials from the conductive carbon network are among the major issues responsible for the capacity degradation of metal oxide/carbon composite electrodes. Various approaches, such as confining the metal oxides between graphene layers[7] and production of small particles,[8] have been adopted to improve the cyclic ability. Better understanding of the effects of crystallinity and particle size on aggregation and separation of metal oxides can offer potential solutions to the issue.

Electrospinning is a facile, one-pot method to synthesize SnO_x/CNF composites with controlled nanostructures of the active material, where SnO_x nanoparticles are uniformly dispersed into the CNF matrix by in situ deposition. The free-standing films obtained after the optimized thermal annealing process can be employed directly as binder-free and conductive additive-free electrodes.[9] The absence of binders will not only increase the energy density, but also avoid the potential

Dr. B. Zhang, J. Huang, Prof. J.-K. Kim
Department of Mechanical and Aerospace Engineering
The Hong Kong University of Science and Technology
Hong Kong, P. R. China
E-mail: mejkkim@ust.hk

DOI: 10.1002/adfm.201501498

detriment of binders on cyclic performance, especial in NIBs where a negative effect of traditional poly(vinylidene fluoride) (PVDF) binder was reported.[10]

There are two important factors that influence the electrochemical performance of SnO_x electrodes, namely crystallization and size of particles. Although much attention has been paid to Li-ion storage behavior of highly crystalline SnO_x particles with several nanometers in diameter,[9,11] relatively few studies have appeared in the literature on amorphous SnO_x since the earlier work tracing back to 1997.[12] As such, amorphous SnO_x electrodes require in-depth understanding of their Li storage behavior and long-term reversibility for widespread applications. The particle size was reported to be of great importance in determining both the specific capacity and cyclic stability, with smaller particles giving rise to better performance.[13] An important issue in using the electrospun CNF composite electrodes is that the SnO_x particles tended to aggregate and drop off from the CNF matrix during the high-temperature carbonization, leading to fast capacity degradation.[11,14] Reduction in SnO_x particle size to a subnanometer level may bring additional benefits to Li- and Na-ion storage. To the best knowledge of the authors, however, no studies have thus far been reported on Na-ion storage in amorphous SnO_x. Therefore, this work aims specifically at enhancing our fundamental understanding of Li- and Na-ion storage mechanisms in ultrafine amorphous SnO_x.

2. Results and Discussion

CNF films with embedded ultrafine amorphous SnO_x particles were synthesized previously,[14] which showed much improved reversibility in LIBs compared to the crystalline SnO_x. In an effort to avoid the separation of SnO_x particles from the CNF matrix, we employed a dual nozzle apparatus in this study to fabricate SnO_x/CNF/CNT composite fibers consisting of a CNF core containing SnO_x particles and a CNF/CNT shell, as shown in **Figure 1**a. A mixture containing polyacrylonitrile (PAN) and Tin(II) 2-ethylhexanoate was used as the core precursor material to introduce amorphous SnO_x within the carbon matrix, instead of creating crystalline SnO_x using a $SnCl_4$ or $SnCl_2$ precursor. The amorphous SnO_x was formed when the Sn ions were bonded with organic groups in tin(II) 2-ethylhexanoate, which prevented SnO_x from crystallization during annealing. A protective shell layer consisting of CNTs in PAN was coated on the tin(II) 2-ethylhexanoate/PAN composite core to avoid the separation of SnO_x particles from the CNF matrix after carbonization (Figure 1b). The X-ray diffraction (XRD) patterns shown in Figure 1c confirm that the SnO_x particles in the composites were totally amorphous. If the fibers were produced using a single nozzle and subjected to the same carbonization process, however, some SnO_x particles were reduced to crystalline Sn, forming a mixed phase of amorphous SnO_x and crystalline Sn in CNFs (Sn/SnO_x/CNF). These SnO_x or Sn crystals tended to agglomerate and drop off from the CNFs because there was no protective coating.[14] To elucidate the role of carbon matrix in preventing the growth and crystallization of SnO_x, neat SnO_x was also prepared without PAN. The XRD pattern of the product (Figure S1, Supporting Information) revealed mixed phases of highly crystalline Sn, SnO, and SnO_2, instead of entirely amorphous SnO_x. The absence of crystalline SnO_x in the XRD pattern of the SnO_x/CNF/CNT composite proves that the shell layer indeed effectively prevented the loss of SnO_x particles. CNTs were added in the shell layer to enhance the electrical conductivity of the fibers. A flexible, freestanding film was obtained, whose electrical conductivity was measured to be 11.3 mS cm^{-1}, about twice that of the SnO_x/CNF composite without CNTs. The chemical state of SnO_x was further investigated by X-ray photoelectron spectroscopy (XPS), finding the presence

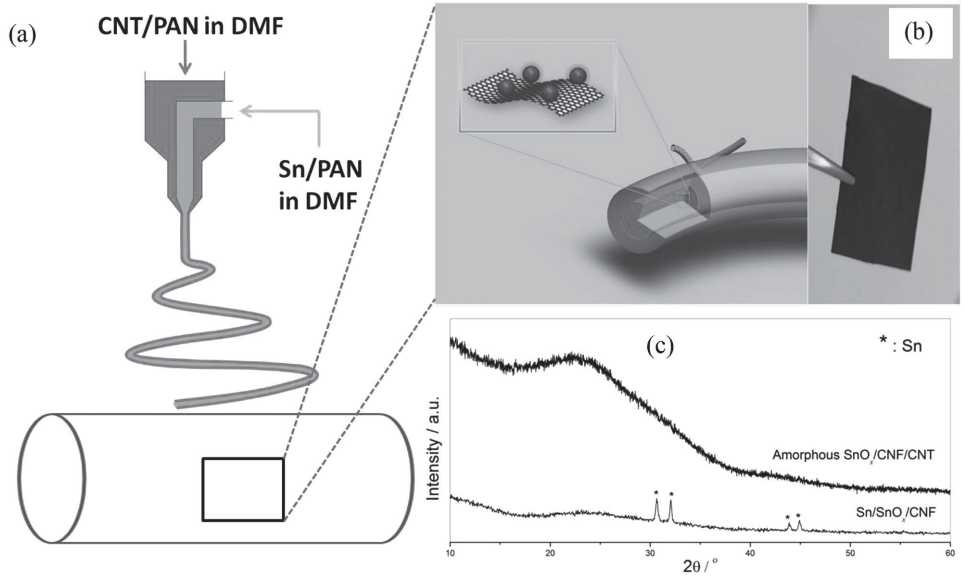

Figure 1. a) Illustration of dual-nozzle electrospinning; b) proposed structure (left) and optical image of freestanding SnO_x/CNF/CNT film (right); and c) XRD patterns of amorphous SnO_x/CNF/CNT and Sn/SnO_x/CNF composites.

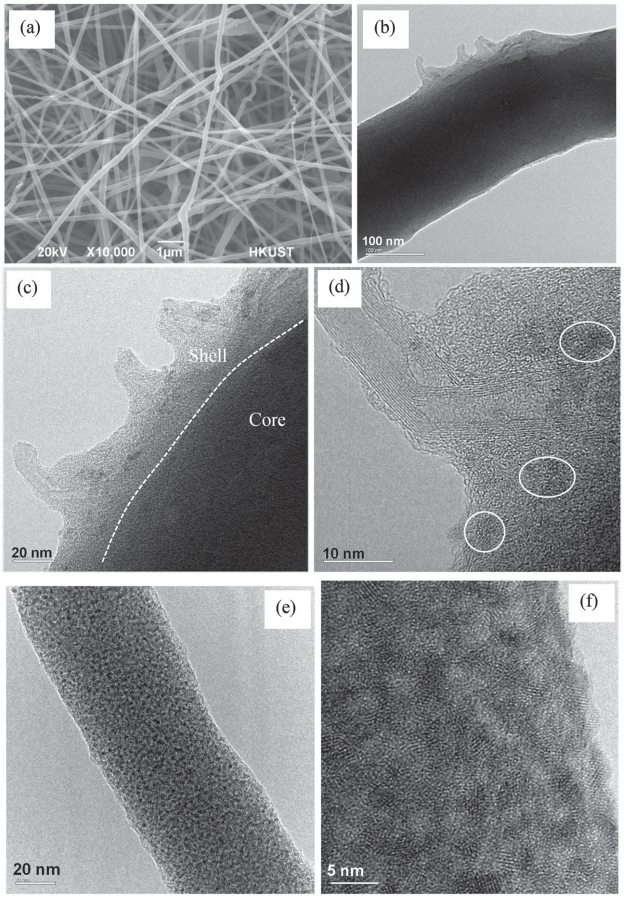

Figure 2. a) SEM image and b–d) TEM images of SnO_x/CNF/CNT composites; the circles in (d) indicate the SnO_x particles in the shell. e,f) TEM images of SnO_x/CNF/CNT composites after thermal annealing at 350 °C for 5 h in air.

of C—O and Sn—O bonds according to the fitted O1s spectrum (Figure S2a, Supporting Information). The spectrum also confirmed the surge of the oxygen level from 3.7 at% in the neat CNFs to 6.9 at% in the SnO_x/CNF/CNT composite. Because the effect of Sn incorporation on oxygen content in CNFs is unknown, the value of x in SnO_x is difficult to estimate. The SnO_x content in the composite was ≈17 wt% based on the thermogravimetric analysis (TGA) results (Figure S2b, Supporting Information).

The scanning electron microscopy (SEM) image of the SnO_x/CNF/CNT composite in **Figure 2**a shows that the CNFs had a smooth surface with their diameters ranging 100–300 nm. There was no evidence of large agglomeration of SnO_x or CNTs. The fibers had a typical core/shell structure with a high contrast in color (Figure 2b,c): the core was much darker than the shell because of the Sn-rich phase in the core. CNTs were embedded in the shell layer with a few CNT tips protruding out (Figure 2d). Several dark SnO_x spots of 1–2 nm in diameter were noted in the shell layer (Figure 2d) which may have been diffused from the core during thermal annealing. They remained in an amorphous state without forming crystal lattices, partly indicating the shell layer to successfully function as a barrier to separation of SnO_x from CNFs. The presence of SnO_x in the core was also proven by element mapping in Figure S3 (Supporting Information), where Sn was scattered over the entire CNFs. In order to visualize the SnO_x particles, the SnO_x/CNF/CNT films were further thermally treated at 350 °C in air so that the carbon shell was partially removed while allowing the overgrowth and crystallization of SnO_x. The results shown in Figure 2e,f present ultrauniform dispersion of crystalline SnO_x particles of 2–3 nm in diameter embedded in CNFs. In light of the overgrown SnO_x particle size, it can be postulated that the pristine, amorphous SnO_x particles present in the SnO_x/CNF/CNT composite on an atomic scale and likely with a subnanometer size.

The Li-ion storage behavior of SnO_x was evaluated using coin cells with metallic lithium as counter electrodes. The CV curves in **Figure 3**a show that a reduction peak at ≈0.75 V appeared in the first cycle due to the formation of a solid electrolyte interface film, which disappeared in the following scans. This led to a large irreversible capacity in the first cycle, resulting in a low Coulombic efficiency of 72%, as shown in Figure 3b. The efficiency surged to 97.5% in the second cycle and further increased to over 99% starting from the fifth cycle. Two redox peaks appeared at around 0.01 and 0.5 V, corresponding to Li insertion/extraction into/from carbon and alloying/dealloying with Sn, respectively. Another oxidation peak present ≈1.2 V is ascribed to the following reaction

$$Sn + Li_2O \leftrightarrow Li + SnO_x \quad (1)$$

which was thought to be irreversible in crystalline SnO_x and became partly reversible in ultrafine SnO_x.[14,15] As a consequence, two plateaus at around 0.5 and 1.2 V were observed in the charge curves of Figure 3b. The charge plateau at above 1 V arose partly from Li storage at the nitrogen-induced defects in carbon, which has a plateau at ≈1.5 V. [16] The high reversibility of SnO_x gave rise to excellent cyclic and rate performance, as shown in Figure 3c,d. The SnO_x/CNF/CNF electrodes delivered a high capacity of 525 mAh g^{-1} when discharged at 0.5 A g^{-1} and maintained equally excellent 345 and 194 mAh g^{-1} when the current density was increased to 4 and 10 A g^{-1}, respectively. An estimation based on the capacity of neat CNFs (≈320 mAh g^{-1} at 0.5 A g^{-1}[16] and the composition of the composites indicates that the ultrafine SnO_x active material contributed ≈50% of the total capacities with only 17 wt% of the electrode. The capacity retention at high current densities was much better than the Sn/SnO_x/CNF composite electrode containing a mixed phase of Sn and SnO_x which was prepared from single-nozzle spinning (Figure S4, Supporting Information). Full utilization of the active, amorphous SnO_x particles without losing crystalline Sn particles by separation from CNFs was mainly responsible for the better performance of the SnO_x/CNF/CNT electrodes. The CNTs incorporated in the shell layer also much contributed to the enhanced electrical conductivity of the electrode, beneficial to fast charge transfer at high current densities. The excellent capacity retention was further verified through long cyclic tests at a high current density of 2 A g^{-1}: a decent capacity of 405 mAh g^{-1} was obtained after 300 cycles.

The Li-ion storage behaviors during the intercalation/extraction process were entirely different between the amorphous

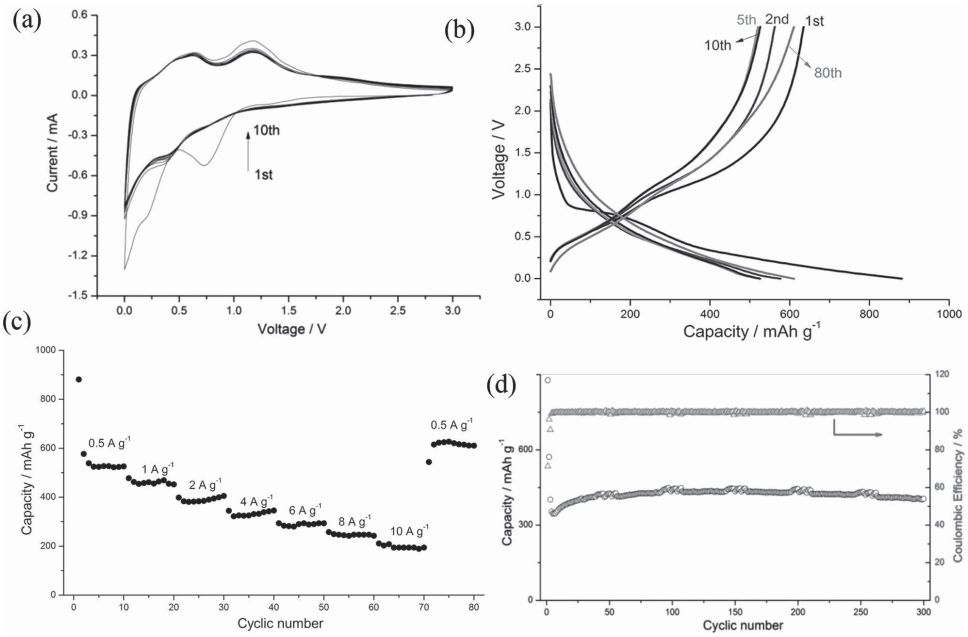

Figure 3. Electrochemical performance of SnO_x/CNF/CNT composite electrodes in LIBs: a) CV curves scanned at 0.2 mv s^{-1}; b) charge/discharge curves at 0.5 A g^{-1}; c) rate performance at different current densities; and d) cyclic performance at 2 A g^{-1}.

and crystalline SnO_x particles. The in situ transmission electron microscopy (TEM)[17] revealed that upon intercalation, the crystalline SnO_2 particles were transformed into Li_2O and $Li_{4.4}Sn$, along with a volume expansion of over 200%, resulting in poor cyclic performance. To gain better understanding of Li-ion storage behavior of amorphous, ultrafine SnO_x particles, their phase transformation, and morphological changes were probed by in situ XRD analysis of a Swagelok-type cell with a beryllium window. The charge/discharge curves of the cell and the corresponding XRD patterns at selected potentials are depicted in **Figure 4**a. The background of electrolyte and separator that had a wide peak at around 20° was not subtracted here for clarity. There was no clear shift of the (002) peak because the Li ions were stored mostly in the disordered graphene sheets and defect sites of CNFs, similar to disordered carbon materials,[18] indicating Li-ion intercalation did not take place. To our surprise, however, no peaks corresponding to Sn/Li_xSn were detected during the full charge/discharge process. Ex situ XRD analysis (Figure S5, Supporting Information) was also conducted to prove the presence of Li_xSn. When the discharged electrode was exposed in air, Li_xSn reacted with O_2 and H_2O to form LiOH, Li_2O, and SnO_x. Upon charge to 3 V, almost all the reaction products were restored to amorphous SnO_x. The two broad peaks at around 21.5° and 30.6° corresponding to Sn arose probably from the small amount of irreversible Li_xSn. It is obvious that both the conversion and alloying reactions of SnO_x occurred all in an amorphous state. This finding is totally different from that of crystalline SnO_x, where crystalline $Li_{4.4}Sn$ particles were formed along with several intermediate phases, such as LiSn and Li_5Sn_2, when discharged to 0 V.[19] It is postulated that the pristine SnO_x active material was not crystallized at all into the ordered Sn during the charge/discharge process. This was confirmed by the ex situ TEM image of SnO_x taken after discharging to 0 V; see Figure 4b,c. The ultrafine SnO_x particles remained in monodispersion without agglomeration after alloying with Li ions and the associated volumetric expansion. Furthermore, they sustained their original amorphous state and kept uniformly distributed within the CNF matrix even after 300 cycles, as shown in Figure 4d and the inset selected area electron diffraction (SAED) pattern. These observations signify a synergistic effect of ultrafine amorphous SnO_x particles firmly embedded in the carbon matrix on inhibiting the growth and crystallization of SnO_x, giving rise to much improved long-term cyclic stability.

Because of its excellent cyclic performance in Li-ion storage, we further explored the potential application of the SnO_x/CNF/CNT composite electrodes in NIBs. The charge/discharge curves shown in **Figure 5**a are similar to those of the crystalline SnO_2 particles. A plateau observed during the oxidation at ≈1.0 V is attributed to the conversion of SnO_x into Sn, while the capacity at below 1.0 V is ascribed to alloying of Sn with Na and the storage of Na ions in disordered graphene layers of CNFs. Another small plateau at ≈2.0 V may stem from the formation of $NaSnO_x$.[4] These plateaus remained quite stable after 45 cycles, proving high reversibility of both the conversion and alloying reactions. The corresponding capacity of the SnO_x/CNF/CNT composite electrode was 280 mAh g^{-1} after 45 cycles at 25 mA g^{-1}, which is not notably high because of the low loading of active SnO_x. However, they delivered an excellent rate capacity and capacity retention at high current densities (Figure 5b,c). High capacities of 219, 182, and 164 mAh g^{-1} were obtained at 250, 1000, and 2000 mA g^{-1}, respectively, which outperformed their counterpart electrodes made from SnO_2/graphene[20] and SnO_2/porous carbon composites.[21]

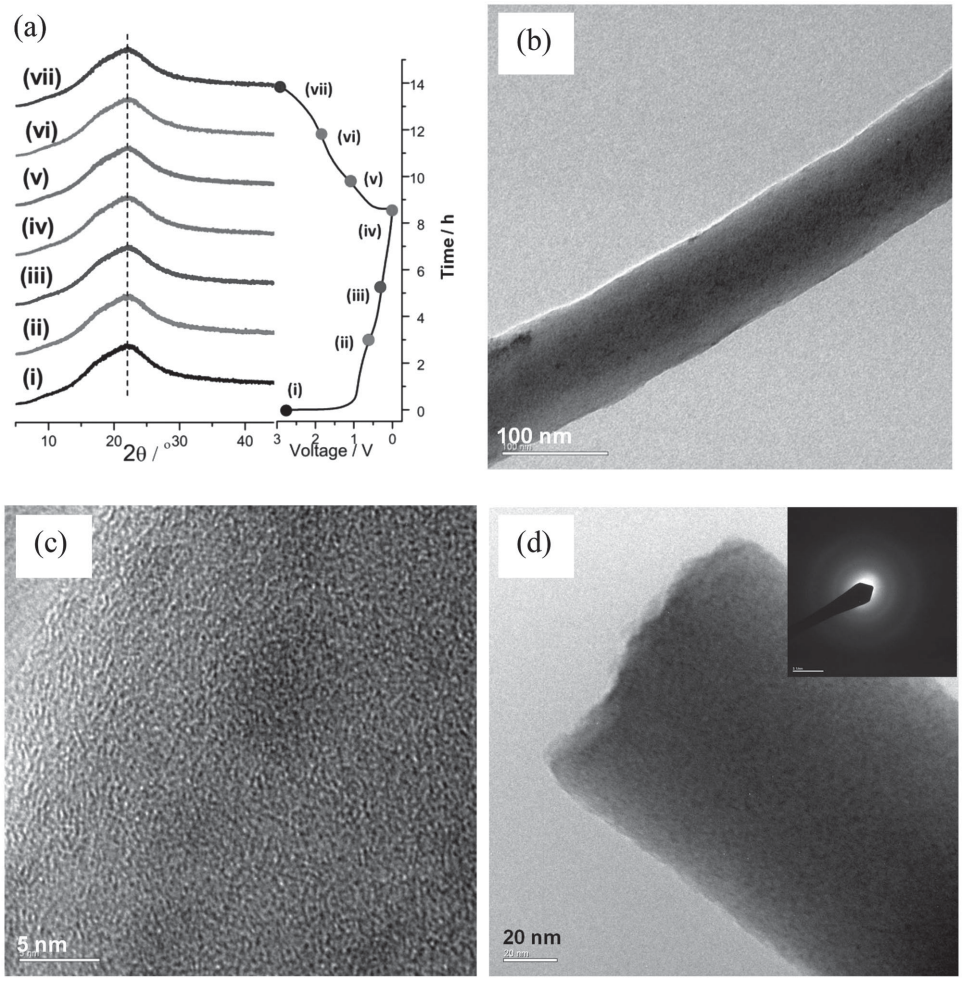

Figure 4. a) In situ XRD patterns at different charge/discharge voltages in LIBs; b) TEM and c) HRTEM images of SnO_x/CNF/CNT electrode discharged to 0 V; and d) a TEM image of SnO_x/CNF/CNT electrode after 300 cycles (charged to 3 V) in LIBs and the corresponding SAED pattern in the inset.

Their cyclic stability was equally excellent with a stable capacity of 210 mAh g^{-1} after 300 discharge cycles at 0.5 A g^{-1} and around 80% retention of its initial capacity. Two ameliorating mechanisms, as discussed above for LIBs, were also responsible for the excellent capacity retention in NIBs. i) The full encapsulation of SnO_x in the CNF matrix effectively alleviated the volume change during the Na-Sn alloying/dealloying process. ii) The uniform distribution of ultrafine SnO_x in CNFs prevented aggregation and crystallization of SnO_x during the charge/discharge cycles. In addition, the neat CNF matrix also contributed a stable capacity of 130 mAh g^{-1}.

The in situ XRD analysis was performed to investigate the phase transformation occurring during Na insertion/extraction, as shown in Figure 5d. No new prominent peaks were detected when discharged to 0 V, confirming that Na_xSn and Na_2O formed during discharge remained in an amorphous state, similar to LIBs. The small peak observed at around 31.5° when charged to 3 V may be due to the side reaction between carbon and electrolyte, which was also noted for a hard carbon anode.[22] In addition, there was no clear shift of the (002) peak for carbon, which is different from the observations for some hard carbon materials carbonized at high temperatures and showing enlarged d-spacing between the graphene layers after intercalation.[23] One possible reason is that the disordered structure of graphene layers arising from the low carbonization temperature of 750 °C used in this work led to the adsorption of Na-ions on the surface of graphene, instead of intercalation.[24]

Major disadvantages of Na-ion storage compared to Li-ion storage in SnO_2 include the sluggish reaction kinetics and the negative role of crystalline Na_2O which in turn prevent charge transfer in the Na_2O/Sn matrix and induce a much larger volume change than in Li_2O. As a consequence, only a small amount of reversible Na, i.e., one Na per SnO_2, could be inserted/extracted.[25] In comparison, we demonstrate here that SnO_x can contribute a stable capacity of 570 mAh g^{-1} for 300 cycles, i.e., approximately three Na per SnO_x. This value was calculated using the capacity difference between the CNF and SnO_x/CNF/CNT composite electrodes (Figure 5c) and taking into account the SnO_x content. Consequently, approximately half the total capacities of the composites were contributed by SnO_x although it only accounted for 17 wt% of the electrode. Apart from the well-dispersed, ultrafine SnO_x particles with

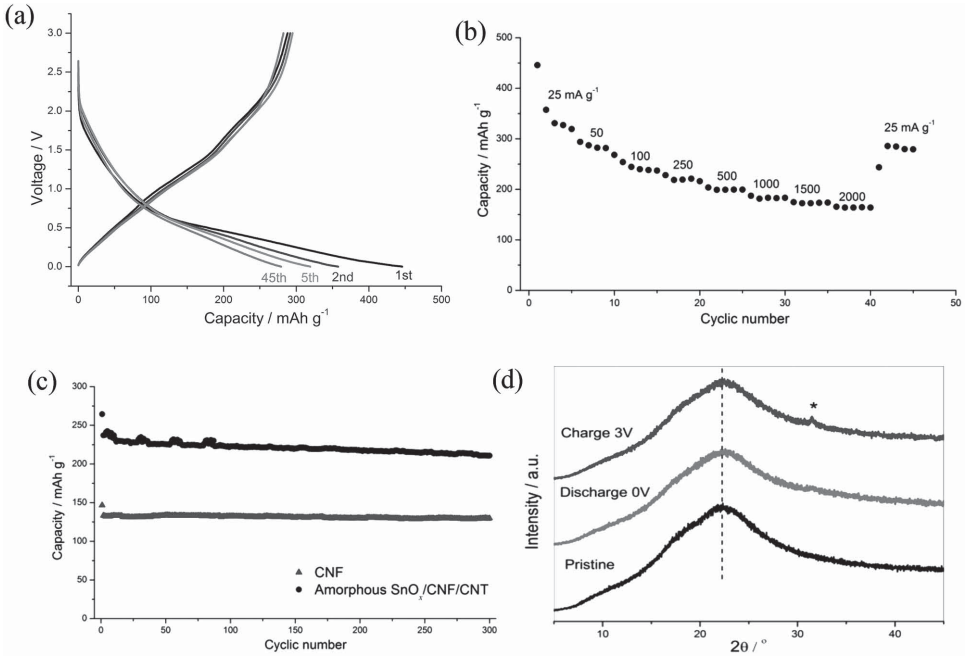

Figure 5. Na-ion storage behaviors of SnO_x/CNF/CNT composite electrodes: a) charge/discharge curves at 25 mA g^{-1}; b) rate performance; c) cyclic stability at 0.5 A g^{-1}; and d) in situ XRD patterns of the cells discharged to 0 V and charged to 3 V.

much reduced volumetric strains and transfer lengths of Na ions that have an inherently low diffusion rate, the amorphous Na_2O avoided the detrimental effect of large crystalline Na_2O on electronic and ionic conductivities.

3. Conclusion

In summary, ultrafine amorphous SnO_x particles embedded in core/shell-structured CNF/CNT fiber films were successfully produced through a dual-nozzle electrospinning. The shell carbon layer containing CNTs functioned as a barrier to avoid the separation of SnO_x which often occurred in SnO_x/CNF electrodes prepared by single-nozzle electrospinning. The incorporation of CNTs enhanced the electrical conductivity of the electrodes by twofold. The in situ XRD analysis revealed that the SnO_x particles presented Li- or Na-ion storage mechanisms totally different from those of the crystalline SnO_x counterparts. The reaction products, like Li_2O and Na_2O, and Li_xSn or Na_xSn alloy sustained in an amorphous state during the whole charge/discharge cycles. They maintained their original ultrafine sizes and uniform distribution in the CNF matrix without growth or agglomeration into large clusters, as proven by ex situ TEM images. As a result, an excellent rate capability and high capacity retention after long cycles were obtained. These findings highlight the advantages of subnanosized and amorphous active particles in improving the electrochemical performance of both LIBs and NIBs. They may also offer insightful understanding and possible solutions to the poor cyclic performance of widely studied metal oxide anode materials that suffer from large volume changes.

4. Experimental Section

30 mg CNTs (supplied by Iljin Nanotech; diameters ranging 10–20 nm and lengths ranging10–50 μm) were dispersed in 12 mL *N,N*-dimethylformamide (DMF) by ultrasonication for 2 h, and the mixture was centrifuged at 1000 rpm for 10 min to remove large agglomerates. 0.6 g PAN was added into the solution and heated at 80 °C for 3 h to prepare the shell precursor solution. The core precursor solution was prepared by mixing 0.6 g PAN and 0.8 g tin(II) 2-ethylhexanoate in 12 mL DMF. A commercial electrospinner (KATO Tech. Co.) with a dual nozzle consisting of core (0.91 mm) and shell (1.5 mm in outer diameter) channels was used forelectrospinning. A high voltage of 18 kV was applied between the nozzle and a drum collector placed at a distance of 15 cm. The feeding rate of both the core and shell solutions was 1 mL h^{-1}, and the drum collector was rotated at a low speed of 0.6 m min^{-1} to produce polymer fiber films with a uniform thickness. The film was stabilized in an oven at 220 °C for 3 h in air and carbonized at 750 °C for 1 h in nitrogen environment to obtain the SnO_x/CNF/CNT composite film.

The details of material characterization and electrochemical tests can be found from the Supporting Information.

Supporting Information

Supporting Information is available from the Wiley Online Library or from the author.

Acknowledgements

This project was financially supported by the Research Grants Council (GRF Projects 613612 and 16212814) and the Innovation and Technology Commission (ITF Project ITS/318/14) of Hong Kong SAR. The authors are grateful to Prof. Jean-Marie Tarascon of Collège de France for assistance with in situ XRD experiments and fruitful

discussion. They also appreciate the technical assistance from the Materials Characterization and Preparation Facilities (MCPF) of HKUST.

Received: April 14, 2015
Revised: May 28, 2015
Published online: July 14, 2015

[1] B. Dunn, H. Kamath, J. M. Tarascon, *Science* **2011**, *334*, 928.
[2] V. Palomares, P. Serras, I. Villaluenga, K. B. Hueso, J. Carretero-González, T. Rojo, *Energy Environ. Sci.* **2012**, *5*, 5884.
[3] W. J. Zhang, *J. Power Sources* **2011**, *196*, 13.
[4] D. Su, C. Wang, H. Ahn, G. Wang, *Phys. Chem. Chem. Phys.* **2013**, *15*, 12543.
[5] B. Zhang, Q. B. Zheng, Z. D. Huang, S. W. Oh, J. K. Kim, *Carbon* **2011**, *49*, 4524.
[6] Z. Wen, Q. Wang, Q. Zhang, J. Li, *Adv. Funct. Mater.* **2007**, *17*, 2772.
[7] Z. Li, W. Lv, C. Zhang, J. Qin, W. Wei, J. J. Shao, D. W. Wang, B. Li, F. Kang, Q. H. Yang, *Nanoscale* **2014**, *6*, 9554.
[8] Y. Liu, N. Zhang, L. Jiao, Z. Tao, J. Chen, *Adv. Funct. Mater.* **2015**, *25*, 214.
[9] L. Zou, L. Gan, F. Kang, M. Wang, W. Shen, Z. Huang, *J. Power Sources* **2010**, *195*, 1216.
[10] K. Dai, H. Zhao, Z. Wang, X. Song, V. Battaglia, G. Liu, *J. Power Sources* **2014**, *263*, 276.
[11] H. R. Jung, W. J. Lee, *J. Electroanal. Chem.* **2011**, *662*, 334.
[12] Y. Idota, T. Kubota, A. Matsufuji, Y. Maekawa, T. Miyasaka, *Science* **1997**, *276*, 1395.
[13] C. Kim, M. Noh, M. Choi, J. Cho, B. Park, *Chem. Mater.* **2005**, *17*, 3297.
[14] B. Zhang, Y. Yu, Z. Huang, Y. B. He, D. Jang, W. S. Yoon, Y. W. Mai, F. Kang, J. K. Kim, *Energy Environ. Sci.* **2012**, *5*, 9895.
[15] P. Lian, X. Zhu, S. Liang, Z. Li, W. Yang, H. Wang, *Electrochim. Acta* **2011**, *56*, 4532.
[16] B. Zhang, Y. Yu, Z.-L. Xu, S. Abouali, M. Akbari, Y. B. He, F. Kang, J. K. Kim, *Adv. Energy Mater.* **2014**, *4*, 1301448.
[17] J. Y. Huang, L. Zhong, C. M. Wang, J. P. Sullivan, W. Xu, L. Q. Zhang, S. X. Mao, N. S. Hudak, X. H. Liu, A. Subramanian, H. Fan, L. Qi, A. Kushima, J. Li, *Science* **2010**, *1515*, 1515.
[18] D. S. Su, R. Schlögl, *ChemSusChem* **2010**, *3*, 136.
[19] Ian A. Courtney, J. R. Dahn, *J. Electrochem. Soc.* **1997**, *144*, 2045.
[20] Y. X. Wang, Y.-G. Lim, M.-S. Park, S.-L. Chou, J. H. Kim, H.-K. Liu, S.-X. Dou, Y.-J. Kim, *J. Mater. Chem. A* **2014**, *2*, 529.
[21] Y. Xu, Y. Zhu, Y. Liu, C. Wang, *Adv. Energy Mater.* **2013**, *3*, 128.
[22] S. Komaba, W. Murata, T. Ishikawa, N. Yabuuchi, T. Ozeki, T. Nakayama, A. Ogata, K. Gotoh, K. Fujiwara, *Adv. Funct. Mater.* **2011**, *21*, 3859.
[23] J. Ding, H. Wang, Z. Li, K. Cui, D. Karpuzov, X. Tan, A. Kohandehghan, D. Mitlin, *Energy Environ. Sci.* **2015**, *8*, 941.
[24] S. Li, J. Qiu, C. Lai, M. Ling, H. Zhao, S. Zhang, *Nano Energy* **2015**, *12*, 224.
[25] J. Gorka, L. Baggetto, J. K. Keum, S. M. Mahurin, R. T. Mayes, S. Dai, G. M. Veith, *J. Power Sources* **2015**, *284*, 1.